

A&A 592, A131 (2016)
 DOI: [10.1051/0004-6361/201527290](https://doi.org/10.1051/0004-6361/201527290)
 © ESO 2016

**Astronomy
&
Astrophysics**

Herschel/HIFI observations of the circumstellar ammonia lines in IRC+10216^{★,★★}

M. R. Schmidt¹, J. H. He², R. Szczerba¹, V. Bujarrabal³, J. Alcolea⁴, J. Cernicharo⁵, L. Decin^{6,7}, K. Justtanont⁸, D. Teyssier⁹, K. M. Menten¹⁰, D. A. Neufeld¹¹, H. Olofsson^{8,12}, P. Planesas⁴, A. P. Marston⁹, A. M. Sobolev¹³, A. de Koter⁷, and F. L. Schöier^{8†}

¹ N. Copernicus Astronomical Center, Rabiańska 8, 87-100 Toruń, Poland

e-mail: schmidt@ncac.torun.pl

² Key Laboratory for the Structure and Evolution of Celestial Objects, Yunnan Observatories, Chinese Academy of Sciences, PO Box 110, Kunming, Yunnan Province, PR China

³ Observatorio Astronómico Nacional. Ap 112, 28803 Alcalá de Henares, Spain

⁴ Observatorio Astronómico Nacional (IGN), Alfonso XII N°3, 28014 Madrid, Spain

⁵ ICMC, CSIC, group of Molecular Astrophysics, C/Sor Juana Inés de la Cruz N3, 28049 Cantoblanco, Madrid, Spain

⁶ Instituut voor Sterrenkunde, Katholieke Universiteit Leuven, Celestijnenlaan 200D, 3001 Leuven, Belgium

⁷ Sterrenkundig Instituut Anton Pannekoek, University of Amsterdam, Science Park 904, 1098 Amsterdam, The Netherlands

⁸ Chalmers University of Technology, Department of Earth and Space Sciences, Onsala Space Observatory, 439 92 Onsala, Sweden

⁹ European Space Astronomy Centre, ESA, PO Box 78, 28691 Villanueva de la Cañada, Madrid, Spain

¹⁰ Max-Planck-Institut für Radioastronomie, Auf dem Hügel 69, 53121 Bonn, Germany

¹¹ Johns Hopkins University, Baltimore, MD 21218, USA

¹² Department of Astronomy, AlbaNova University Center, Stockholm University, 10691 Stockholm, Sweden

¹³ Ural Federal University, Astronomical Observatory, 620000 Ekaterinburg, Russian Federation

Received 1 September 2015 / Accepted 23 May 2016

ABSTRACT

Context. A discrepancy exists between the abundance of ammonia (NH₃) derived previously for the circumstellar envelope (CSE) of IRC+10216 from far-IR submillimeter rotational lines and that inferred from radio inversion or mid-infrared (MIR) absorption transitions.

Aims. To address the discrepancy described above, new high-resolution far-infrared (FIR) observations of both ortho- and para-NH₃ transitions toward IRC+10216 were obtained with *Herschel*, with the goal of determining the ammonia abundance and constraining the distribution of NH₃ in the envelope of IRC+10216.

Methods. We used the Heterodyne Instrument for the Far Infrared (HIFI) on board *Herschel* to observe all rotational transitions up to the $J = 3$ level (three ortho- and six para-NH₃ lines). We conducted non-LTE multilevel radiative transfer modelling, including the effects of near-infrared (NIR) radiative pumping through vibrational transitions. The computed emission line profiles are compared with the new HIFI data, the radio inversion transitions, and the MIR absorption lines in the ν_2 band taken from the literature.

Results. We found that NIR pumping is of key importance for understanding the excitation of rotational levels of NH₃. The derived NH₃ abundances relative to molecular hydrogen were $(2.8 \pm 0.5) \times 10^{-8}$ for ortho-NH₃ and $(3.2^{+0.7}_{-0.6}) \times 10^{-8}$ for para-NH₃, consistent with an ortho/para ratio of 1. These values are in a rough agreement with abundances derived from the inversion transitions, as well as with the total abundance of NH₃ inferred from the MIR absorption lines. To explain the observed rotational transitions, ammonia must be formed near to the central star at a radius close to the end of the wind acceleration region, but no larger than about 20 stellar radii (1σ confidence level).

Key words. stars: AGB and post-AGB – circumstellar matter – stars: carbon – stars: individual: IRC+10216

1. Introduction

Ammonia (NH₃) was the first polyatomic molecule discovered in space (Cheung et al. 1968), and has subsequently been one of the most extensively observed molecules in the interstellar medium

* *Herschel* is an ESA space observatory with science instruments provided by European-led Principal Investigator consortia and with important participation from NASA. HIFI is the *Herschel* Heterodyne Instrument for the Far Infrared.

** The reduced spectra (FITS files) are only available at the CDS via anonymous ftp to cdsarc.u-strasbg.fr (130.79.128.5) or via <http://cdsarc.u-strasbg.fr/viz-bin/qcat?J/A+A/592/A131>

† Deceased 14 January 2011.

(Ho & Townes 1983), with a set 23 GHz of inversion transitions that are readily detectable from many radio telescopes. Emission lines resulting from these transitions are widely detected in the dense parts of both dark and star-forming molecular clouds (see e.g. Harju et al. 1993; Jijina et al. 1999; Wienen et al. 2012). Because ammonia is a symmetric top molecule, an analysis of its excitation allows the effects of temperature and density to be determined separately; as a result, the metastable lines of ammonia are often used to derive the temperature and density of dense clumps in molecular clouds. (Walmsley & Ungerechts 1983; Danby et al. 1988; Kirsanova et al. 2014).

Ammonia has also been detected in the circumstellar envelopes of evolved stars, but has been observed less extensively

in such environments than in the interstellar medium. Several absorption features in the ν_2 vibration–rotational bands around $10\ \mu\text{m}$ were detected in some asymptotic giant branch (AGB) stars, as well as in a few massive supergiants (Betz et al. 1979; McLaren & Betz 1980; Betz 1987). At about the same time, the $1.3\ \text{cm}$ wavelength inversion transitions of ammonia were detected from C-rich AGB and post-AGB stars (Betz 1987; Nguyen-Q-Rieu et al. 1984, 1986).

In IRC+10216 (CW Leo), ammonia was observed for the first time by its infrared absorption lines in the ν_2 band around $10\ \mu\text{m}$ (Betz et al. 1979), and its detection in radio inversion transitions was announced shortly thereafter (Bell et al. 1980). In the following years, new observations of IRC+10216 were performed in both infrared absorption (Keady & Ridgway 1993; Monnier et al. 2000) and radio inversion lines (Kwok et al. 1981; Bell et al. 1982; Nguyen-Q-Rieu et al. 1984; Gong et al. 2015).

IRC+10216 was detected in the Two-micron Sky Survey as the brightest infrared sky object at $5\ \mu\text{m}$ outside the solar system (Becklin et al. 1969), and soon its heavily obscured central star was identified as being C-rich based on the presence of strong CN absorption bands (Herbig & Zappala 1970; Miller 1970). Presently, IRC+10216 is the best studied C-rich AGB star. About half of the molecules detected in space are seen in the envelope of this source, due to its proximity (distance, d , of $130\ \text{pc}$, see Menten et al. 2012) and a relatively large mass loss rate $\sim 1\text{--}4 \times 10^{-5}\ M_{\odot}\ \text{yr}^{-1}$ (e.g. Groenewegen et al. 1998; Truong-Bach et al. 1991).

The development of heterodyne technology for observations in the far-infrared (FIR) enabled the first detection of the $1_0(\text{s})\text{--}0_0(\text{a})$ rotational transition of ortho- NH_3 by the *Odin* satellite toward IRC+10216 (Hasegawa et al. 2006), which was followed by the detection of the same transition in some O-rich AGB stars and red-supergiants (Menten et al. 2010) by the Heterodyne Instrument for the Far Infrared (HIFI, de Graauw et al. 2010) on board the *Herschel* Space Observatory (*Herschel*, Pilbratt et al. 2010). Furthermore, by fully exploiting the capabilities of the HIFI instrument, we were able to observe all nine rotational transitions up to the $J = 3$ levels of ortho- and para- NH_3 (this paper) in the envelope of IRC+10216.

There is a clear discrepancy between the estimated amount of para- NH_3 relative to molecular hydrogen in IRC+10216 derived from radio inversion lines (3×10^{-8} ; Kwok et al. 1981) and that of ortho- NH_3 derived from its lowest rotational line (about 10^{-6} ; Hasegawa et al. 2006). Nevertheless, both values, which lie within the range of ammonia abundances observed towards other C-rich and O-rich stars, and cannot be explained by standard chemical models (see discussion in Menten et al. 2010). However, the chemical model presented recently by Decin et al. (2010) seems able to reproduce the high abundance of ammonia observed in IRC+10216 (see their Fig. 3). Their model, constructed with the aim of explaining the presence of water vapour in the envelope of this C-rich star, assumes a clumpy envelope structure, where a fraction of the interstellar UV photons is able to penetrate deep into the envelope and dissociate mostly ^{13}CO , providing oxygen for O-rich chemistry in the inner warm parts of a C-rich circumstellar envelope. On the other hand, Neufeld et al. (2013) have suggested, on the basis of H_2O isotopic ratios, that a recent model invoking shock chemistry (Cherchneff 2012) may provide a more successful explanation for the presence of water in envelopes of C-rich stars. However, this model does not provide information on the ammonia formation.

In this paper we present new *Herschel*/HIFI observations of nine rotational transitions of NH_3 (three ortho and six para lines),

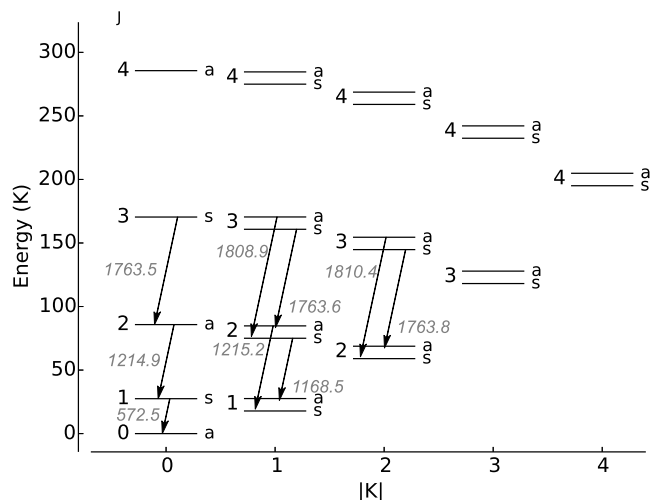


Fig. 1. Diagram of energy levels of ortho- ($|K| = 0, 3$, etc.) and para- NH_3 ($|K| = 1, 2, 4$, etc.). The inversion splitting between levels of different symmetry is exaggerated for clarity. The observed rotational transitions with frequencies in GHz are indicated with arrows.

eight of which have been detected for the first time, and an analysis of their implications with the use of detailed modelling.

The observations and data reduction are presented in Sect. 2. Section 3 is devoted to the description of the molecular structure of ammonia, while Sect. 4 presents details of the modelling procedure and the best fits found for all rotational transitions. In Sect. 5 we discuss the results thereby obtained and their consequences. Finally, a summary of this study is presented in Sect. 6.

2. Observations

Observations of IRC+10216 were carried out with the *Herschel*/HIFI instrument as part of the HIFISTARS Guaranteed Time Key Program (Proposal Id: KPGT_vbujarra_1; PI: V. Bujarrabal); in addition, a spectral line survey has been carried out for this object (Proposal Id: GT1_jcernich_4; PI: J. Cernicharo). The observed rotational lines of ortho- and para- NH_3 are listed in Table 1 and indicated in Fig. 1, which shows the diagram of the lowest rotational levels of ammonia. For each observed transition, Table 1 gives the line identification, its frequency in GHz, the corresponding HIFI band, the energy of the upper level in K, the *Herschel* OBSERVATION ID, the date of the observation, the optical phase (ϕ) of the observation (counted from the reference maximum phase of the light curve, $\phi = 0$, on Julian date JD = 2454554 with an assumed period of 630 days (Menten et al. 2012)), the half power beam width (HPBW) of the *Herschel* telescope at the observed frequency, the main beam efficiency η_{mb} , the integrated flux in K km s^{-1} with its estimated uncertainty, and the observing mode: single tuning or spectral scan. In this paper, we analyse wide band spectrometer (WBS) data only.

The HIFI observations of IRC+10216 were reduced with the latest version of HIPE (13.0) with data processed with Standard Product Generator (SPG) version 13.0.0. The data were processed using the HIPE pipeline to level 2, which was set to provide intensities expressed as the main beam temperature. Main beam efficiencies were taken from the recent measurements by Mueller et al. (2014)¹. They differ by up to 20% from the older

¹ http://herschel.esac.esa.int/twiki/pub/Public/HifiCalibrationWeb/HifiBeamReleaseNote_Sep2014.pdf

Table 1. Summary of NH₃ observations in IRC+10216.

Transition ^a	Frequency (GHz)	Band	E_u^b (K)	<i>Herschel</i> OBSID	Obs. date	Phase ^c	HPBW	η_{mb}	Int. flux (K km s ⁻¹)	Observing mode
1₀(s)-0₀(a)	572.498	1b	29	1342195794	2010-05-04	0.22	37.5''	0.62	22.7 ± 1.2	single point
				1342196413	2010-05-11	0.22				single point
2 ₁ (s)-1 ₁ (a)	1168.452	5a	58	1342196514	2010-05-13	0.23	18.2''	0.59	19.5 ± 2.0	spectral scan
2₀(a)-1₀(s)	1214.853	5a	86	1342196514	2010-05-13	0.23	17.5''		39.2 ± 3.9	spectral scan
2 ₁ (a)-1 ₁ (s)	1215.246	5a	60	1342196514	2010-05-13	0.23	17.5''		21.8 ± 2.2	spectral scan
3₀(s)-2₀(a)	1763.524	7a	170	1342233281	2011-11-28	0.13	12.0''	0.58	48.5 ± 7.2	single point
3 ₁ (s)-2 ₁ (a)	1763.601	7a	143	1342233281	2011-11-28	0.13	12.0''		23.7 ± 3.6	single point
3 ₂ (s)-2 ₂ (a)	1763.823	7a	127	1342233281	2011-11-28	0.13	12.0''		23.2 ± 2.3	single point
3 ₁ (a)-2 ₁ (s)	1808.935	7b	144	1342196574	2010-05-15	0.23	11.7''	0.58	18.0 ± 9.0	spectral scan
3 ₂ (a)-2 ₂ (s)	1810.380	7b	128	1342196574	2010-05-15	0.23	11.7''		18.1 ± 9.0	spectral scan

Notes. ^(a) Ortho transitions and their frequencies are indicated in bold face. ^(b) Energies of levels for para-NH₃ should be increased by 22 K if put on the common energy scale with ortho-NH₃. ^(c) Counted from the reference maximum phase of the light curve, $\phi = 0$ on Julian date JD = 2 454 554, and period of 630 days (Menten et al. 2012).

determinations by Roelfsema et al. (2012). Frequencies are always given in the frame of the local standard of rest (LSR).

The statistical uncertainties in the integrated line fluxes, as derived formally from the rms noise in the spectra (see below) are relatively small, while it is known that systematic uncertainties in the HIFI flux calibration are much larger (Roelfsema et al. 2012). Therefore, somewhat arbitrarily, we have assumed a 5% uncertainty in the integrated line flux for lines observed in band 1b, a 10% uncertainty for lines in bands 5a and 7a, and a 50% uncertainty for lines in band 7b. However, since two of the lines observed in band 7a are blended (see below), we increased the assumed uncertainty in their integrated flux from 10 to 15%. The method used to deconvolve line blends and to derive individual line fluxes is described in Sect. 2.2. The observed line profiles are shown by the solid lines in Fig. 2.

2.1. Single point observations

The HIFISTARS observations were all performed in the dual beam switch (DBS) mode. In this mode, the HIFI internal steering mirror chops between the source position and two positions located 3' on either side of the science target. There are two entries in Table 1 for the ground-state transition 1₀(s)-0₀(a) of ortho-NH₃, since these two observations were made with slightly shifted local oscillator frequencies. This procedure was adopted to confirm the assignment of any observed spectral feature to either the upper or lower sideband of the HIFI receivers (Neufeld et al. 2010). The resultant spectra were co-added since no contamination was found to originate from the other side band. Spectra obtained for the horizontal (H) and vertical (V) polarizations were found to be very similar (differences smaller than 5%) and were co-added too. After resampling to a channel width of 1 km s⁻¹, the final baseline rms noise in the coadded spectra was 6 mK in band 1b and 40 mK in band 7a.

2.2. Spectral scan observations

We made use of data from the full spectral scan of IRC+10216 (GT1_jcernich_4 by Cernicharo et al., in prep.) to obtain measurements of five additional transitions of ammonia observed in two bands, 5a and 7b (see Table 1). The spectral scan observing mode allows for the unique reconstruction of the single-sideband spectrum in a wide spectral range at the price of significantly lower signal-to-noise ratio. Spectral scan observations were also

made in dual beam switch mode with fast chop. Both the spectral resolution and signal-to-noise ratio are lower for these observations than for the single point ones. Lines observed in the scan mode were deconvolved to obtain a single-sideband spectrum. To reduce the noise in the profiles, the final spectra were resampled to 1 km s⁻¹ in band 5a and 2 km s⁻¹ in band 7b. The final rms noise in the resampled spectra was 125 mK and 200 mK in bands 5a and 7b, respectively.

The para-NH₃ transition 3₁(s)-2₁(a) at 1763.601 GHz (middle panel) overlaps the ortho-NH₃ transition 3₀(s)-2₀(a) at 1763.524 GHz (upper left panel). Therefore, the shape of the former line was approximated in its blueshifted part using, as a template, a properly rescaled profile of the para-NH₃ 3₂(s)-2₂(a) emission line (middle right panel), which was observed with the same beam size and has a similar excitation. The line profile of the ortho-NH₃ transition 3₀(s)-2₀(a) was then obtained by subtracting the derived para-NH₃ 3₁(s)-2₁(a) line emission. The resulting profiles are shown by dot-dashed lines in Fig. 2.

2.3. Other observations

To verify our best fit models, we used radio and mid-infrared data for ammonia available from the literature. In this paper, we exploited radio data from Gong et al. (2015), who recently observed five metastable inversion transitions (J, K) = (1, 1), (2, 2), (3, 3), (4, 4), (6, 6) of ortho- and para- ammonia in a 1.3 cm line survey toward IRC+10216. The dates of those observations correspond to phases, ϕ , from about ~ 0.62 to ~ 0.97 (Gong et al. 2015). The half power beam width amounts to 40'' at the frequency of the inversion lines (about 24 GHz) for observations with the Effelsberg 100 m radio telescope (Gong et al. 2015). Flux densities, S_ν in Jy, were converted to main beam temperature T_{mb} , in K, using the conversion factors suggested by the authors: $T_{\text{mb}}/S_\nu = 1.33$ K/Jy for the (6, 6) line at 25 GHz and $T_{\text{mb}}/S_\nu = 1.5$ K/Jy for the remaining lines.

By way of comparison with the mid-infrared absorptions of ammonia, we used profiles of the ν_2 transitions published by Keady & Ridgway (1993) that were observed at a spectral resolution of 0.009 cm⁻¹ (corresponding to 2.9 km s⁻¹) with the Fourier Transform Spectrometer at the Coudé focus of the 3.8 m Kitt Peak Mayall telescope. Observations of absorption from the metastable rotational levels within the ground vibrational level of ortho- and para-ammonia, $aR(0, 0)$, $aQ(2, 2)$, $aQ(3, 3)$, $aQ(4, 4)$, $aQ(6, 6)$ were also used for comparison with the results of our

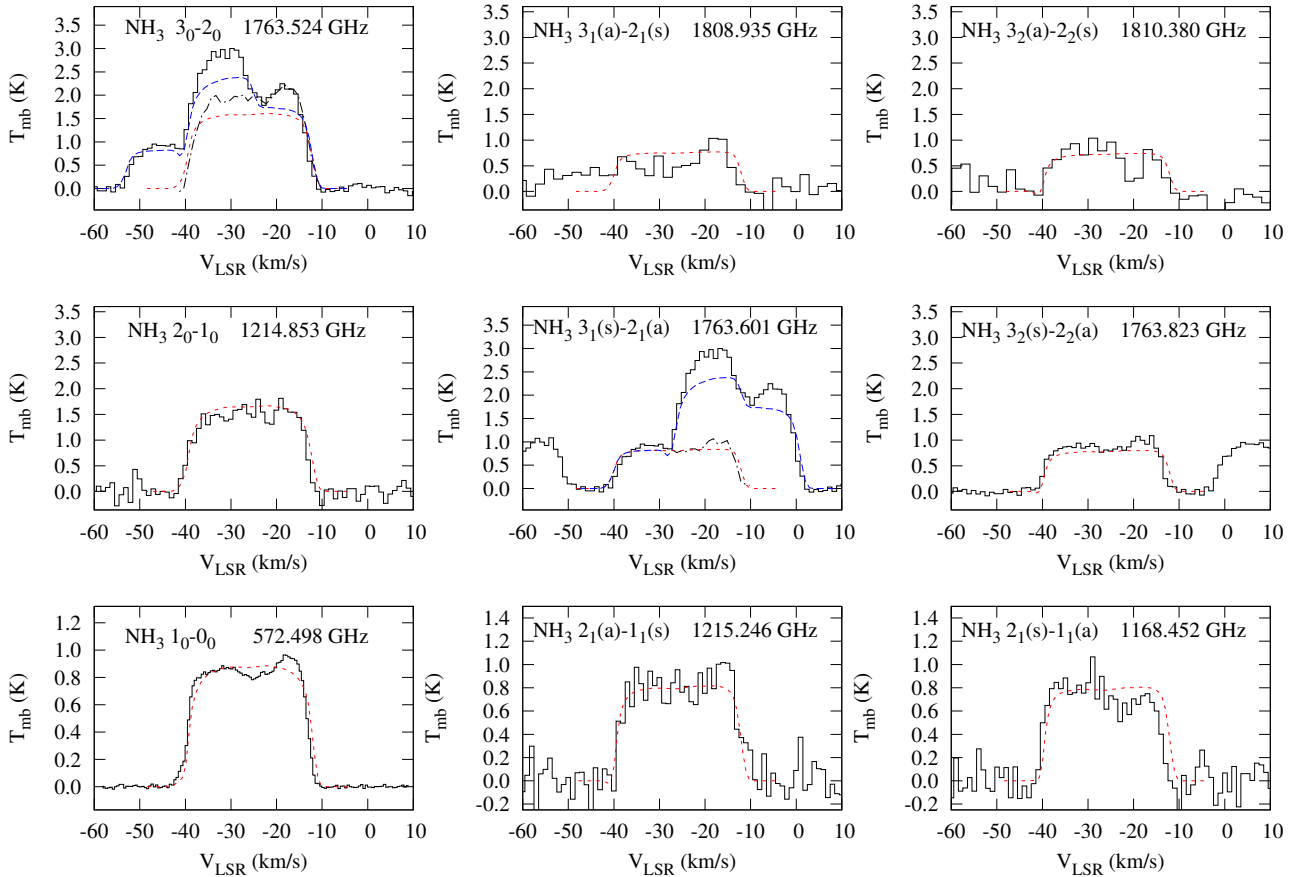


Fig. 2. HIFI observations of rotational transitions of ortho-NH₃ (*left column*) and para-NH₃ (*middle and right columns*) are shown by solid lines. Approximated line profiles (see Sect. 2.2) of two blended lines 3₀(s)–2₀(a) and 3₁(s)–2₁(a) are shown by dot-dashed lines. Emission profiles are overlapped with theoretical profiles (red dashed lines) from our best fit models computed separately for each ammonia spin isomer. The effect of line overlapping in case of the two blends is shown with blue dashed lines. The theoretical profiles for the three lines that were observed at phase $\phi = 0.13$ (see Table 1) are rescaled up to mimic computations at phase $\phi = 0.23$ (see Sect. 4.5 for details). Our approach in searching for the best fit is described in Sect. 4.5, and the best fitting parameters are compiled in Table 2.

modelling. Formally, from the aperture of the telescope, we can estimate the HPBW to be $0''.67$, using the expression $1.22 \times \lambda/D$, where λ is wavelength and D is diameter of the telescope aperture. However, taking into account all instrumental effects, we estimate that the HPBW, in this case, could be as large as $1''$.

3. Ammonia model

Different relative orientations of the spins of the three hydrogen nuclei give rise to two distinct species of NH₃: ortho and para. The general criterion governing which levels belong to ortho- and which to para-ammonia is formulated in terms of representations of the molecular symmetry group (see Bunker & Jensen 1998). According to this formalism, ortho states belong to the A'_2 and A''_2 representations of the inversional symmetry group D_{3h} , and para states to the E' and E'' representations. For the electronic ground state of ammonia, this translates into the rule that ortho-NH₃ has levels with $K = 3n$, where $n = 0, 1, \dots$, and para-NH₃ has all other levels. The two species do not interact either radiatively or collisionally. The ortho- to para-NH₃ ratio is determined at the moment of the formation of the molecule. Hence, we consider ortho- and para-ammonia as separate molecular species. Transitions of the two species whose frequencies overlap, such as the ortho-NH₃ 3₀(s)–2₀(a) transition and the para-NH₃ 3₁(s)–2₁(a) transition, open the possibility of an interaction

through the emission and absorption of line photons. This is considered further in the discussion below.

Ammonia may oscillate in six vibrational modes: the symmetric stretch ν_1 , symmetric bend ν_2 , doubly-degenerate asymmetric stretch ν_3^j , and the doubly-degenerate asymmetric bend ν_4^j . Transitions from the ground vibrational state to each of these excited states are observed as vibrational bands at 3, 10, 2.9, and 6 μm , respectively. The band intensities are characterized by the vibrational transition moments 0.027, 0.24, 0.018, and 0.083, respectively (Yurchenko et al. 2011). As long as we consider only the lowest excited vibrational modes, the rule governing the assignment of levels of given K to the ortho and para species, discussed above for the ground state, is preserved for the rotational levels of the symmetric modes and exchanged for the asymmetric ones.

The vibrational ground state of ammonia is split into two states of opposite parities, a consequence of the low energy barrier to inversion of the molecule. Symmetry considerations exclude half of the rotational levels for the $K = 0$ ladder. Only transitions with $\Delta K = 0$ are electric dipole-allowed. As a result, there is a characteristic doubling of rotational transitions allowed between levels of opposite parities for transitions with $K \neq 0$. Forbidden transitions ($\Delta K \neq 0$) are significantly weaker. Transitions between split sub-levels are allowed as well and give rise to a large number of lines around 23–25 GHz, the so called inversion

lines. Their hyperfine structure (hfs) splitting may be neglected in the rotational and vibrational transitions but does influence the line profiles for inversion lines although for IRC+10216, the maximal spread of the hfs components is smaller than the CSE's expansion velocity. Moreover, the intensities of hfs satellite features relative to that of the main feature (at the central frequency) only become appreciable if an inversion transition (with possible exception of the (1, 1) transition) attains significant optical depth.

The list of transitions and their strengths was extracted from the recent BYTe computations (Yurchenko et al. 2011). In the initial analysis, we extended the sets of molecular data for ortho- and para-NH₃ compiled in the LAMDA database (Schöier et al. 2005) by adding energy levels for the excited vibrational states. Two data sets were explored, the first one with only the $\nu_2 = 1$ levels, and the second one with $\nu_1 = 1$, $\nu_2 = 1$ and $\nu_3 = 1$, and $\nu_4 = 1$ levels. The rotational quantum numbers of the vibrational levels were limited to those originally used in the ground state, i.e. $J, K \leq 7$, 7 in ortho- and $J, K \leq 5$, 6 in para-ammonia. Both dipole ($\Delta K = 0$) and forbidden ($\Delta K \neq 0$) transitions between the levels were included.

We found that the inclusion of the $\nu_2 = 1$ rovibrational states has a dramatic effect on the flux predicted for the observed pure rotational transitions, when compared with predictions obtained without the inclusion of vibrationally excited states. However, the additional inclusion of the $\nu_1 = 1$, $\nu_2 = 2$, $\nu_3 = 1$, and $\nu_4 = 1$ vibrational states has a negligible effect on the computed fluxes for the observed transitions, a maximum increase of only 2 percent being obtained for the flux of the ground rotational transition of ortho-NH₃ with even smaller increases for the remaining emission lines. This conclusion, which is based on a model of a molecular structure limited to rotational levels up to $J = 7$ in each vibrational state, is explained by the fact that the vibrational transition moments to the symmetric bending state are significantly higher than those to the remaining vibrational states. In fact, the radiative pumping rate in the ν_2 mode dominates over radiative pumping rates in the remaining modes, even in the innermost parts of the envelope where shorter-wavelength radiation prevails. At larger distances from the star, dust opacity decreases the photon density at shorter wavelengths more effectively, further reducing the relative effect of radiative pumping in other modes. The IR pumping effects for ammonia have been investigated previously by Schöier et al. (2011) and Danilovich et al. (2014).

Solving the radiative transfer, we do not distinguish between photons produced in the envelope and photons coming from the central star. However, by comparing the radiative rates from our best fit model with those obtained when only stellar photons are present, we were able to estimate their relative importance. Only in the inner part of the envelope is radiative excitation in the ν_2 transition dominated by the stellar photons. Very quickly, already at seven stellar radii the contribution from the envelope begins to prevail over the contribution from the central star, reaching a ratio of twenty at the outer edge.

Our final model for ammonia includes all levels up to $J = 15$ in both the vibrational ground state and the $\nu_2 = 1$ vibrational state, amounting to a total of 172 levels and 1579 transitions for ortho-NH₃ and 340 levels and 4434 transitions for para-NH₃. We include the ground state and vibrational levels up to 3300 cm⁻¹, corresponding to 4750 K, above ground. The completeness of the levels used in the computations may be judged by comparing the partition function calculated for the model with that obtained from the full list of lines from the BYTe computations (Yurchenko et al. 2011). With the number of levels given

above, the partition function for the ortho species is equal to the BYTe number for temperatures to 300 K, and is lower by 2%, 28%, and 40%, respectively, at 600, 1000, and 1200 K. The partition function of para species is also complete up to 300 K, and is lower by 10%, 40%, and 55%, respectively, at 600, 1000, and 1200 K. The incompleteness in the levels may result in an overestimate of their populations in the dense and hot inner parts of the envelope.

We adopted the collisional rate coefficients from Danby et al. (1988). The rate coefficients for collisional de-excitation are available only for low-lying levels below $J = 6$ and for a maximum temperature of 300 K. Collisional rates were extrapolated to higher temperatures with a scaling proportional to the square root of the gas temperature. The extension of collisional rates to other levels is necessarily quite crude. At first we neglected collisional rates between levels not available in Danby's work. In this case, the ladder of levels with K higher than 6 in ortho-ammonia and higher than 5 in para-ammonia are populated only by forbidden radiative transitions. To analyse the influence of the unknown collisional rates on the excitation of NH₃, we carried out additional computations based on crude estimates of the collisional rates; here, we adopted collisional depopulation rates of 10⁻¹¹ or 10⁻¹⁰ cm³ s⁻¹ for rotational states in the ground vibrational state, and rates of 10⁻¹⁴ cm³ s⁻¹ for excited vibrational states. None of these approximations seem to significantly influence our conclusions inferred from the modelling of the observed transitions.

4. Modelling

Here, we present our numerical code and then describe all the assumptions made and parameters investigated during our search for the best fits to the observed rotational transitions of ammonia. After that, we describe the method used to search for the best fit to the data, and present the results thereby obtained.

4.1. Numerical code and procedures

To model circumstellar absorption and emission lines, we developed a numerical code, MOLEXCSE (Molecular Line EXcitation in CircumStellar Envelopes), to solve the non-LTE radiative transfer of molecular lines and the dust continuum. Here, the methodology was to consistently include the effects of optical pumping by the central star and infrared pumping by circumstellar dust upon the population of the molecular levels. The first effect is more critical in the case of post-AGB stars, and the second one more important in AGB stars (see e.g. Truong-Bach et al. 1987). The effect of the dust on the radiation intensity inside the envelope is included by solving the radiative transfer for the line and continuum radiation. For this purpose, the critical properties of the dust – the coefficients of extinction, scattering, and thermal emission – are determined by a separate code by modelling the observed spectral energy distribution of the source, as described in Sect. 4.4. Reproducing the observed continuum fluxes allows the absorption line profiles for mid-infrared vibrational transitions to be computed.

The radiative transfer equation is formulated in the comoving frame (Mihalas et al. 1975) to include the effects of an expanding spherical shell. The only difference is the linearization of the differential equations along tangent rays on a geometrical grid instead of on grid of optical depths. The purpose of this modification was to avoid numerical problems when maser or laser transitions emerge during the iterations.

The simultaneous solution of the statistical equilibrium equations and of the radiative transfer in lines is a non-linear process and, to be efficient, requires linearization of the equations. Full linearization of the radiative transfer equation is very complex and its solution is time-consuming. In the code we follow the approach presented by [Schoenberg & Hempe \(1986\)](#). The original formulation of their approximate Newton-Raphson operator was modified to include the geometrical formulation of radiative transfer mentioned above.

The program possesses two additional features useful in the application to ammonia. First, it enables the simultaneous solution of the radiative transfer problem for more than one molecule. Second, the radiative transfer may be solved with the inclusion of line overlap effects between different molecules. With these features, one can consistently compute the effects of line blending between ortho- and para-NH₃. The prominent example of such a case is the overlap between rotational transitions of para-NH₃ 3₁(s)–2₁(a) and of ortho-NH₃ 3₀(s)–2₀(a).

In computing the profiles of the inversion lines, we resolved the hyperfine structure of ammonia, including the effects of quadrupole and magnetic splitting, as measured by [Kukolich \(1967\)](#) and updated by [Rydbeck et al. \(1977\)](#). Line strengths were computed when necessary using the formula given by [Thaddeus et al. \(1964\)](#). These theoretical line strengths are in good agreement with the observed intensities both in laboratory experiments ([Kukolich 1967](#)) and in observations of molecular clouds ([Rydbeck et al. 1977](#)). The magnetic splitting is much smaller than the quadrupole splitting and has little effect on the line profiles and therefore was neglected in our computations. When solving the radiative transfer, the populations of the sublevels are distributed according to the statistical weights, i.e. assuming local thermodynamical equilibrium (LTE) between sublevels. The relative LTE ratios of intensities as defined by [Osorio et al. \(2009\)](#) were applied including effects of line overlap. The code has been tested by comparison with previously published models of AGB circumstellar envelopes. A detailed description of our code and the tests we conducted will be published elsewhere.

4.2. Thermal and density structure of the envelope

The detailed structure of IRC+10216's envelope has been the subject of many studies. We mention here only those based on the analysis of CO emission lines ([Crosas & Menten 1997](#); [Schöier et al. 2002](#); [Agúndez et al. 2012](#); [De Beck et al. 2012](#)) or the spectral energy distribution (e.g. [Men'shchikov et al. 2001](#)).

Several models for the thermal structure have been proposed to explain the CO emissions from IRC+10216. These models differ in the assumed distance, mass loss rate and variation of gas velocity in the inner parts of the envelope. For the purpose of this paper, we have chosen, for the basic temperature structure of the envelope, the model of [Crosas & Menten \(1997\)](#), but with the distance reduced from 150 to 130 pc following [Groenewegen et al. \(2012\)](#) (see also [Menten et al. 2012](#)). The gas temperature structure of [Crosas & Menten \(1997\)](#) is based on self-consistent computations of the temperature structure and radiative transfer in CO, constrained by observations of CO emissions up to $J = 6-5$. The adopted distance, expansion velocity and mass loss rate are listed in [Table 2](#) and the gas temperature structure, T_{gas} , is presented in the upper panel of [Fig. 3](#) by the solid line. The temperature profile has been extended to the inner part of the envelope by assuming a constant value of 1200 K. More recently, [De Beck et al. \(2012\)](#) used the GASTRoNOoM model ([Decin et al. 2006, 2010](#)) to derive the

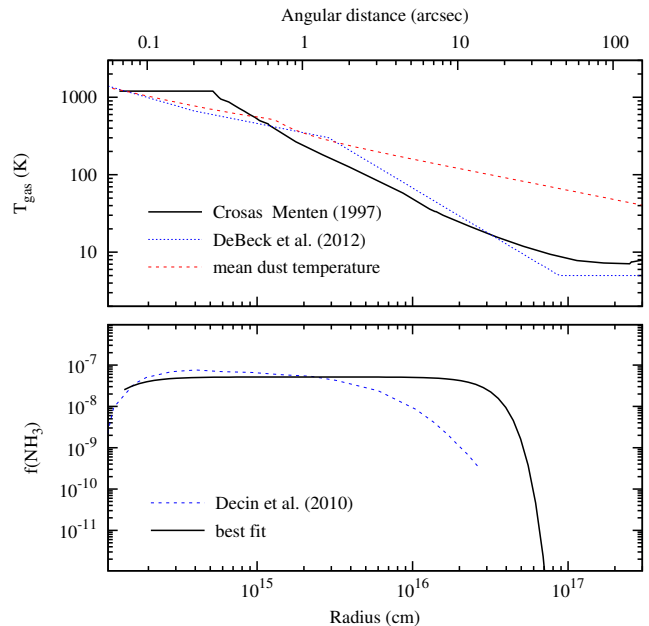


Fig. 3. Gas temperature within the envelope of IRC+10216 adopted for this work (*upper panel*) from [Crosas & Menten \(1997\)](#) is shown by a solid line, while that from [De Beck et al. \(2012\)](#) is shown by a blue dotted line. The dust temperature is shown by a red dashed line. The *lower panel* shows the distribution of ammonia from our best fitting models (solid line), and its theoretical distribution (dashed line) from [Decin et al. \(2010\)](#). The angular distance is given in the top axis of the *upper panel* for an assumed distance to IRC+10216 of 130 pc.

gas temperature structure shown by the dashed line in the upper panel of [Fig. 3](#), and found it capable of explaining HIFI observations of CO up to $J = 16-15$. [Figure 3](#) shows these representative T_{gas} models to have distinct temperature structures, which differ mainly in the middle part of the envelope.

The density structure of the envelope is computed from the equation of mass conservation, assuming that the gas is entirely composed of molecular hydrogen and that the mass loss rate and outflow velocity are constant. The microturbulent velocity was set to be constant throughout the envelope and equal to 1.0 km s^{-1} ([Crosas & Menten 1997](#)). In fact this value seems to explain the observed shape of the lowest ortho-NH₃ 1₀(s)–0₀(a) emission well.

4.3. Distribution of ammonia

The distribution of ammonia in the circumstellar envelope is governed by the poorly-understood process of ammonia formation, and the well-understood process of its photodissociation in the outer part of the envelope. A detailed chemical model predicting the formation of ammonia and water as a result of photo-processes in IRC+10216 was proposed by [Agúndez et al. \(2010\)](#) (see also [Decin et al. 2010](#)). This model predicts peak abundances of ammonia within the observed values but, as we show below, in its present version cannot explain the observed intensities of the rotational transitions.

For the purpose of this paper, we assumed that in the middle parts of the envelope the maximum abundance of ammonia relative to H₂, f_0 , is constant, while in the inner and outer layers it is increasing and decreasing, respectively. To distinguish between ortho- and para-ammonia, their individual abundances are further designated $f(\text{ortho-NH}_3)$ and $f(\text{para-NH}_3)$. The abundance profile adopted for the ammonia in the inner layers is

based on the model of Decin et al. (2010) (see their supplementary material). For each kind of ammonia, we parametrized the increase of its abundance in the inner parts of the envelope by two free parameters: the formation radius, R_f , and f_0 . To describe the increase in the ammonia abundance in the inner envelope, we used a fit to the predictions of Decin et al. (2010) of the form $f(r) = f_0 \times 10^{-0.434(R_f/r)^3}$, where r is radial distance from the central star. This parametrization, despite its theoretical origin, is a more realistic description of the ammonia distribution than a rather unphysical sharp increase of the ammonia abundance at a fixed radius. We note that R_f may be formally lower than the inner dust shell radius. To describe the decrease in the ammonia abundance near the photodissociation radius, R_{ph} , in the outer layers of the envelope, we used the analytical parametrization $f(r) = f_0 \times \exp(-\ln 2(r/R_{ph})^\alpha)$, which is frequently used in a parametrization of CO photodissociation (see e.g. Schöier & Olofsson 2001). A slope $\alpha = 3.2$ was adopted here, in accord with the fit to a detailed chemical model of NH₃ photodissociation computed using the CSENV code by Mamon et al. (1988). The ortho- and para-ammonia abundances, the inner radius of ammonia formation, R_f , and its photodissociation radius, R_{ph} , are free parameters in the fitting procedure. The distribution of ammonia from our best-fit models and from Decin et al. (2010) are shown in Fig. 3 by the solid and dashed lines, respectively.

4.4. Dust shell model of IRC+10216

As explained in Sect. 3, the excitation of ammonia is dominated by radiative pumping via the $10 \mu\text{m}$ $\nu_2 = 1$ band. Therefore, to model the ammonia lines we need to estimate the continuum flux at $10 \mu\text{m}$ inside the whole envelope. For that purpose, we used a dust radiative transfer model (Szczerba et al. 1997), which is able to provide all necessary physical variables to MOLEXCSE. We fit a combination of flux measurements from the Guide Star Catalogue ver. 2.3 (GSC 2.3) for $\lambda < 1 \mu\text{m}$, photometric data between 1.25 and $5 \mu\text{m}$ from Le Bertre (1992), and at longer wavelengths from IRAS and COBE DIRBE. In addition, as the strongest constraint, we have used ISO Short Wavelength Spectrograph (SWS) and Long Wavelength Spectrograph (LWS) spectra. They were obtained on May 31 1996 (JD = 2450235) and correspond to phase ϕ of 0.24, counted from the reference maximum phase of the light curve, $\phi = 0$, on November 17 1988 (JD = 2447483), and given a period of 649 days (Men'shchikov et al. 2001). We have used this older parameterization of the IRC+10216 variability as it was obtained closer to the date of the ISO observations. For this phase of pulsation and the distance of 130 pc determined recently by Groenewegen et al. (2012), the average luminosity of IRC+10216 was estimated to be about $8500 L_\odot$ (Men'shchikov et al. 2001; Menten et al. 2012).

As dust constituents, we adopted amorphous carbon of AC type from Rouleau & Martin (1991) and SiC from Pegourie (1988), both with a power-law distribution of grain radii with an index of -3.5 between 0.1 and $0.43 \mu\text{m}$. We assumed a maximum allowed dust temperature of 1300 K. We assumed a constant outflow velocity equal to the observed terminal velocity of 14.5 km s^{-1} , in spite of a clear variation of the outflowing velocity in the inner part of envelope seen in higher molecular transitions (Agúndez et al. 2012), and a constant dust mass loss rate. The derived dust mass loss rates were $1.0 \times 10^{-7} M_\odot \text{ yr}^{-1}$ and $3.0 \times 10^{-9} M_\odot \text{ yr}^{-1}$ for AC and SiC dust, respectively. The inner shell radius corresponding to the assumed maximum dust

Table 2. Model for IRC+10216.

Parameter	Value
Distance	$d = 130 \text{ pc}$
Expansion velocity	$v_{\text{exp}} = 14.5 \text{ km s}^{-1}$
Mass loss rate (total hydrogen)	$\dot{M} = 3.25 \times 10^{-5} M_\odot \text{ yr}^{-1}$
Stellar radius	$R_\star = 3.9 \times 10^{13} \text{ cm}$
Effective temperature	$T_{\text{eff}} = 2300 \text{ K}$
Luminosity (average)	$L_{\text{avg}} = 8500 L_\odot$
Luminosity at maximum	$L_{\text{max}} = 11850 L_\odot$
Inner shell radius	$1.2 \times 10^{14} \text{ cm}$ ($\sim 3 R_\star$)
<i>Best-fit parameters:</i>	
Formation radius R_f	$1.0 \times 10^{14} \text{ cm}$ ($\sim 2.5 R_\star$)
Photodissociation radius R_{ph}	$> 2-3 \times 10^{16} \text{ cm}$
$f(\text{ortho-NH}_3)$	$(2.8 \pm 0.5) \times 10^{-8} (\frac{3.25 \times 10^{-5}}{M})$
$f(\text{para-NH}_3)$	$(3.2^{+0.7}_{-0.6}) \times 10^{-8} (\frac{3.25 \times 10^{-5}}{M})$

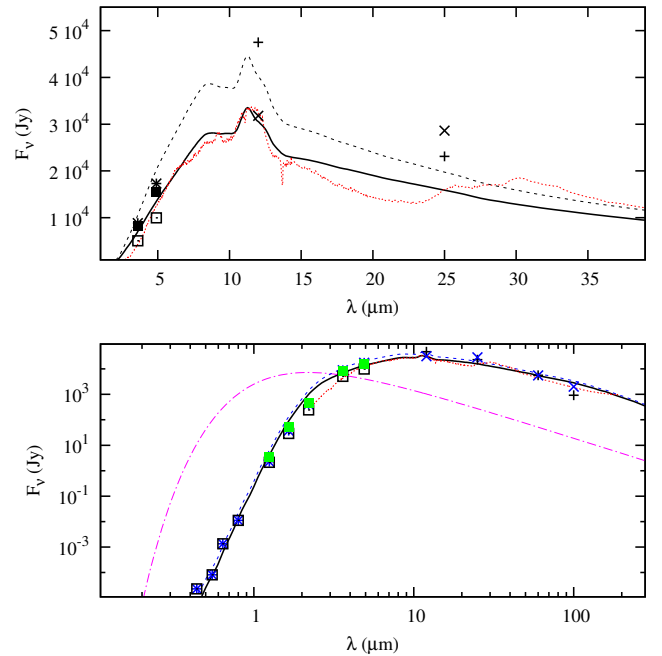


Fig. 4. Fit to the flux for $L_{\text{avg}} = 8500 L_\odot$ and effective temperature of 2300 K is shown in both panels by black solid line. The contribution from the central star is shown in the bottom panel by the dash-dotted magenta line. SWS and LWS ISO spectra are shown by red dotted lines. Photometric data below $1 \mu\text{m}$ are from GSC 2.3, those between 1.25 and $5 \mu\text{m}$ are from Le Bertre (1992) at three different phases: 0.02 (stars), 0.21 (filled squares) and 0.23 (dotted squares), while at longer wavelengths the flux is from IRAS (crosses) and COBE DIRBE (x) measurements. The dust model obtained for $L_{\text{max}} = 11850 L_\odot$ is shown by dashed lines on each panel (see text for details).

temperature is reached at a distance of about 3 stellar radii. The required total optical depth of the envelope at V is 18.5 mag, which corresponds to $\tau_{10 \mu\text{m}}$ equal to 0.18. The parameters of our model for ammonia in IRC+10216 are listed in Table 2 and the mean dust temperature is shown by red dashed line in Fig. 3. As is shown below, the dust temperature determines the radiation intensity in the continuum, which is important for vibrational pumping.

The fit obtained for a stellar luminosity $L_{\text{avg}} = 8500 L_\odot$ and an effective temperature of 2300 K is shown in both panels of Fig. 4 by the black solid line. In our modelling, we did

not include MgS, which is commonly used for modelling of the 30 μm structure, since this material has no optical constants in the optical range so the precise determination of its temperature is impossible (see e.g. [Szczerba et al. 1997](#)). However, since we are interested in the continuum emission at 10 μm , this approach seems to be justified.

Most of the ammonia lines were observed at phase $\phi = 0.23$ (see Table 1), when the luminosity of the central star was close to its average value $L_{\text{avg}} = 8500 L_{\odot}$. However, three of the lines were observed at $\phi \sim 0.13$ so, for the purpose of ammonia line modelling, we rescaled their observed integrated area down to $\phi = 0.13$ using the predicted variability from models obtained at maximum and at average luminosity. Since we do not have ISO spectra taken at $\phi = 0$, we cannot constrain the dust properties at the maximum stellar luminosity. Therefore, we decided to recompute our dust model by keeping all parameters (including the inner radius of dust shell) constant, except for the stellar luminosity, which was raised to L_{max} . The model results thereby obtained are shown by dashed lines in both panels of Fig. 4.

After modelling the dusty envelope, we exported the dust thermal emission coefficient, along with the total extinction and scattering coefficients, to the code MOLEXCSE, as a function of wavelength and radial distance. MOLEXCSE, which was described above in Sect. 4.1, was then used to solve the multi-level radiative transfer in lines and continuum. See Eq. (1) in [Szczerba et al. \(1997\)](#) for details concerning the exported physical quantities.

4.5. The best-fit models

Using our code described in Sect. 4.1, the ammonia abundance profile given in Sect. 4.3, the model parameters specified in Table 2, together with the gas temperature distribution from [Crosas & Menten \(1997\)](#) and, taking into account vibrational pumping by infrared radiation, we computed a grid of separate models for ortho-NH₃ and para-NH₃. The grid of models was computed for formation radii $R_f = 2.5, 5, 10, 20, 40,$ and $80 R_{\star}$, photodissociation radii R_{ph} ranging from 1.5×10^{16} cm to 6×10^{16} cm in steps of $\Delta R_{\text{ph}} = 0.5 \times 10^{16}$ cm, and $f(\text{ortho-NH}_3)$ and $f(\text{para-NH}_3)$ ranging from 1.4×10^{-8} to 4.8×10^{-8} in steps of $\Delta f(\text{NH}_3) = 0.2 \times 10^{-8}$.

For each model we defined the figure-of-merit as

$$\chi^2 = \sum_{i=1, N_{\text{lines}}} \left(\frac{F_i^{\text{obs}} - F_i^{\text{th}}}{\sigma_i} \right)^2, \quad (1)$$

where F_i^{obs} (see Table 1) and F_i^{th} are the observed and theoretically predicted integrated fluxes for the i th line, respectively, σ_i (see Table 1) is the estimated uncertainty in F_i^{obs} , and N_{lines} is 3 for ortho- and 6 for para-NH₃ (see Fig. 2). Here, the three lines observed in 2011 at phase $\phi = 0.13$ were rescaled to phase $\phi = 0.23$, assuming that they vary co-sinusoidally between the maximum and average luminosity of the central star. From the computed integrated line fluxes for these stellar luminosities, we obtained the amplitude of their variations as 4.0, 3.1, and 8.2 K km s⁻¹ for the transitions at 1763.524, 1763.601, and 1763.823 GHz, respectively. Since the value of the cosine function describing ϕ decreases by about 0.6 between phase 0.13 and 0.23, we reduced the integrated fluxes given in Table 1 by 0.6 times the estimated amplitude of the line variations, i.e. by 2.4, 1.9, and 5.0 K km s⁻¹. The quality of each fit is measured by the reduced χ^2 parameter, which for two free parameters is defined here as $\chi_{\text{red}}^2 = \chi^2 / (N_{\text{lines}} - 2)$.

We found that for $R_{\text{ph}} \geq 3 \times 10^{16}$ cm, the minimum value of χ_{red}^2 is achieved for $R_f = 2.5 R_{\star} = 1.0 \times 10^{14}$ cm, which is the minimum formation radius possible for the assumed inner radius of the envelope considered during modelling. However, since the assumed R_{ph} is decreased, the formation radius that minimizes χ_{red}^2 increases (from $R_f = 10 R_{\star}$ for $R_{\text{ph}} = 2.5 \times 10^{16}$ cm to $R_f = 40 R_{\star}$ for $R_{\text{ph}} = 1.5 \times 10^{16}$ cm); at the same time, however, the minimum χ_{red}^2 also increases. Hence, the value of the photodissociation radius was found by searching for the minimum χ_{red}^2 among the models for $R_f = 2.5 R_{\star}$.

The best fit to the ortho-NH₃ lines is achieved for $R_{\text{ph}} > 2-3 \times 10^{16}$ cm, and $f(\text{ortho-NH}_3) = (2.8 \pm 0.5) \times 10^{-8}$ at a 3σ confidence level. There is no strong constraint on the maximum value that R_{ph} could have. To estimate the errors, we constructed a χ^2 map for ortho-NH₃, which is presented in the left panel of Fig. 5, and shows how χ^2 varies as a function of the photodissociation radius R_{ph} and $f(\text{ortho-NH}_3)$ for the best-fit formation radius $R_f = 1.0 \times 10^{14}$ cm. The contours correspond to 1, 2, and 3σ confidence limits. The best fit is indicated with the cross and the corresponding value of $\chi_{\text{red}}^2 = 1.2$ is shown on the plot. Rotational transitions of para-NH₃ are even less sensitive to the photodissociation radius, and a plot similar to that shown on left panel of Fig. 5 does not yield any constraints on R_{ph} . This behaviour could be related to the fact that at a given distance from the star the pumping mid-IR radiation is the same, while at low gas temperatures the excitation of the $1_0(s)-0_0(a)$ transition of ortho-ammonia is much more efficient than the excitation of the $2_1(s)-1_1(a)$ transition of para-ammonia (see Fig. 1). On the other hand, the lowest para-NH₃ transition, $2_1(s)-1_1(a)$, was observed with HPBW of 18.2'', corresponding to a projected radius of 1.8×10^{16} cm at the assumed distance of 130 pc; thus, for values of R_{ph} that are larger than this projected radius, this line is less sensitive to R_{ph} than the $1_0(s)-0_0(a)$ ortho-NH₃ transition, for which the HPBW is twice as large.

The derived abundance of para-NH₃ for the best-fit model is $(3.2_{-0.6}^{+0.7}) \times 10^{-8}$, which means that, to within the error bars, the ratio of ortho- to para-NH₃ is equal to 1, a ratio that is characteristic of the formation of NH₃ at high temperatures ([Umamoto et al. 1999](#)). The average abundance for the two species is $(3.0 \pm 0.6) \times 10^{-8}$. The error estimate for the para-NH₃ abundance given above is the 3σ confidence interval obtained from the χ^2 map for para-NH₃, which is presented in the middle panel of Fig. 5 and shows how χ^2 varies as a function of the formation radius R_f and abundance of para-NH₃ at the best-fitting photodissociation radius $R_{\text{ph}} = 3 \times 10^{16}$ cm. The meaning of the contours is the same as in the left panel. The best fit, indicated with the cross, and the corresponding χ_{red}^2 are also shown on the plot. The minimum χ_{red}^2 of 0.5 implies an excellent fit to the six para-NH₃ lines (with four degrees of freedom).

While the χ^2 analysis described above made use of integrated line fluxes instead of the detailed line profiles, the model successfully reproduces the line shapes. The emission line profiles resulting from the best-fit models are shown in Fig. 2 by dashed lines, and the best-fit parameters are listed in Table 2. As indicated in Table 2, the abundances derived for ortho- and para-NH₃ are inversely proportional to the assumed mass-loss rate; this can be understood as a consequence of the facts that the NH₃ lines are optically thin and that the derived ammonia abundance is only weakly dependent on the exact choice of the gas temperature (see below), so the same total mass of ammonia is required to explain the observations regardless of the mass-loss rate.

To check how strongly the derived best-fit parameters depend on the assumed gas temperature inside the envelope, we

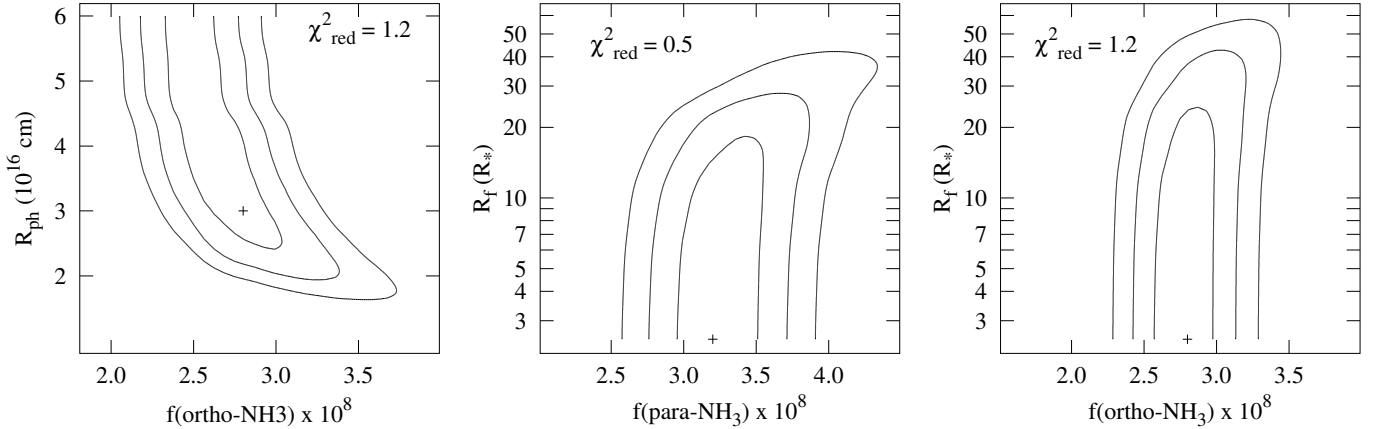


Fig. 5. Contours of χ^2 , indicating the sensitivity of the fit to the model’s free parameters. The *left panel* shows the dependence of χ^2 on the photodissociation radius R_{ph} and abundance of ortho-NH₃, given the best fitting value for the formation radius, $R_{\text{f}} = 2.5 R_{\star}$. The *middle and right panels* show the dependence of χ^2 on the formation radius R_{f} and the abundances of para- and ortho-NH₃, given a photodissociation radius $R_{\text{ph}} = 3 \times 10^{16}$ cm. The contours correspond to 1, 2, and 3σ confidence levels. The best fits are marked with a cross and the corresponding χ_{red}^2 are shown on the plots.

performed some test computations using the T_{gas} structure from De Beck et al. (2012). For the best fitting parameters found above and the T_{gas} structure of De Beck et al. (2012), we found that the line shapes are only slightly different, but χ_{red}^2 increases to 3.8 for ortho- and to 4.6 for para-NH₃. Searching for the model minimizing χ_{red}^2 , we found that the best fit is obtained for a formation radius $R_{\text{f}} = 1 \times 10^{14}$ cm, a photodissociation radius $R_{\text{ph}} = 3 \times 10^{16}$ cm, and abundances of ortho-NH₃ and para-NH₃ equal to $(3.0^{+0.6}_{-0.5}) \times 10^{-8}$ and $(3.6^{+0.8}_{-0.7}) \times 10^{-8}$, respectively. These values lie within the error bounds estimated using the Crosas & Menten (1997) temperature profile, implying that the abundances and photodissociation radius derived from rotational transitions are only weakly dependent on the choice of temperature profile.

Although we obtained the best-fit results based solely on rotational transitions, our model also offers predictions for the other observed transitions. Therefore to make a quality test of our best-fit models, we examined whether they can reproduce both the inversion and mid-IR transitions of ammonia.

While Gong et al. (2015) have obtained observations of the inversion transitions at several different phases (in range 0.20–0.96), our models do not predict any dependence on the integrated fluxes in the phase (i.e. luminosity) of the central star. Calculations show that the expected variation of flux in the (1, 1) inversion line is up to 3 percent between phases of maximum ($\phi = 0$) and mean ($\phi = 0.25$), and is even lower in higher inversion transitions. Thus, our model computed for the average luminosity of the star can be used for comparison with the inversion line observations. Figure 6 shows the observed transitions by means of solid lines (Gong et al. 2015) and the computed theoretical profiles with dashed lines. Vertical sticks mark positions of hyperfine components – the height of the central stick is chosen arbitrary, while the heights of the other sticks are scaled according to their relative theoretical intensities. Our best-fit model for the rotational transitions fits the upper inversion transitions very well, but overestimates the flux measured for the para-NH₃ (2, 2) line, and significantly overestimates that for the lowest para-NH₃ (1, 1) line. We have found that decreasing R_{ph} to 1.5×10^{16} cm gives a very good fit to the all observed inversion lines (shown by dotted lines in Fig. 6). However, this model is not able to match the rotational lines as successfully as our best-fit model. Using the best-fit abundance of ortho-NH₃ and decreasing the photodissociation radius to 1.5×10^{16} cm

significantly increases the χ_{red}^2 , to a value 28. On the other hand, the best-fit model with fixed $R_{\text{ph}} = 1.5 \times 10^{16}$ cm and free formation radius and abundance of ortho-NH₃ moves R_{f} to about $40 R_{\star}$ and $f(\text{ortho-NH}_3)$ to 4.2×10^{-8} with χ_{red}^2 equal to 3.8.

To investigate this discrepancy, we extended the search for the best-fit model by adding the inversion lines. To this purpose, we took the integrated flux from Gong et al. (2015) and converted it to K km s^{-1} scale. However, our theoretical fit to the inversion lines seems to suggest the presence of hyperfine components, as we describe below in Sect. 5.4 of discussion, at least in the case of the two lowest inversion lines, (1, 1) and (2, 2). Therefore, we repeated the calculation of the integrated flux of these two lines, extending the integration range accordingly. This increased the integrated flux of those two transitions up to about 20% in case of the (1, 1). The integrated fluxes used for the analysis of the inversion lines for ortho-NH₃ (3, 3) and (6, 6) transitions are 0.47 ± 0.5 and $0.15 \pm 0.03 \text{ K km s}^{-1}$, respectively, while for the para-NH₃ (1, 1), (2, 2), and (4, 4) transitions are 0.84 ± 0.8 , 0.64 ± 0.9 , and $0.20 \pm 0.4 \text{ K km s}^{-1}$, respectively. Now, considering simultaneously the inversion and rotational lines of para-NH₃ put a strong constraint on the photodissociation radius. For the formation radius fixed to the $R_{\text{f}} = 1.0 \times 10^{14}$ cm, we found that the photodissociation radius is $R_{\text{ph}} = (1.5 \pm 0.2) \times 10^{16}$ cm and the abundance of para-NH₃ $f(\text{para-NH}_3) = (3.2 \pm 0.5) \times 10^{-8}$ with χ_{red}^2 equal to 0.86. However, the same approach for ortho-NH₃ gives rather a different estimation of the photodissociation radius, which is equal to $(5^{+1}_{-3}) \times 10^{16}$ cm and the abundance of ortho-NH₃ equal to $(2.4 \pm 0.4) \times 10^{-8}$ with χ_{red}^2 equal to 1.9. Thus, we see, that a global fit gives ortho- and para-NH₃ abundances that are quite similar (within error bars) to those obtained from the analysis limited to the rotational lines only. However, the problem of requiring different photodissociation radii for ortho- and para-NH₃ remains.

The infrared transitions to the ν_2 levels are seen in absorption against the background dust continuum emission. The observed depths of lines depend on the telescope beam size. In addition, the line spectrum is smoothed by the instrumental profile. The observed ν_2 line profiles published by Keady & Ridgway (1993) and synthesized using our best-fit models are shown in Fig. 7. There is reasonable consistency between our model results (dashed line) with the observed profiles (solid line). Some

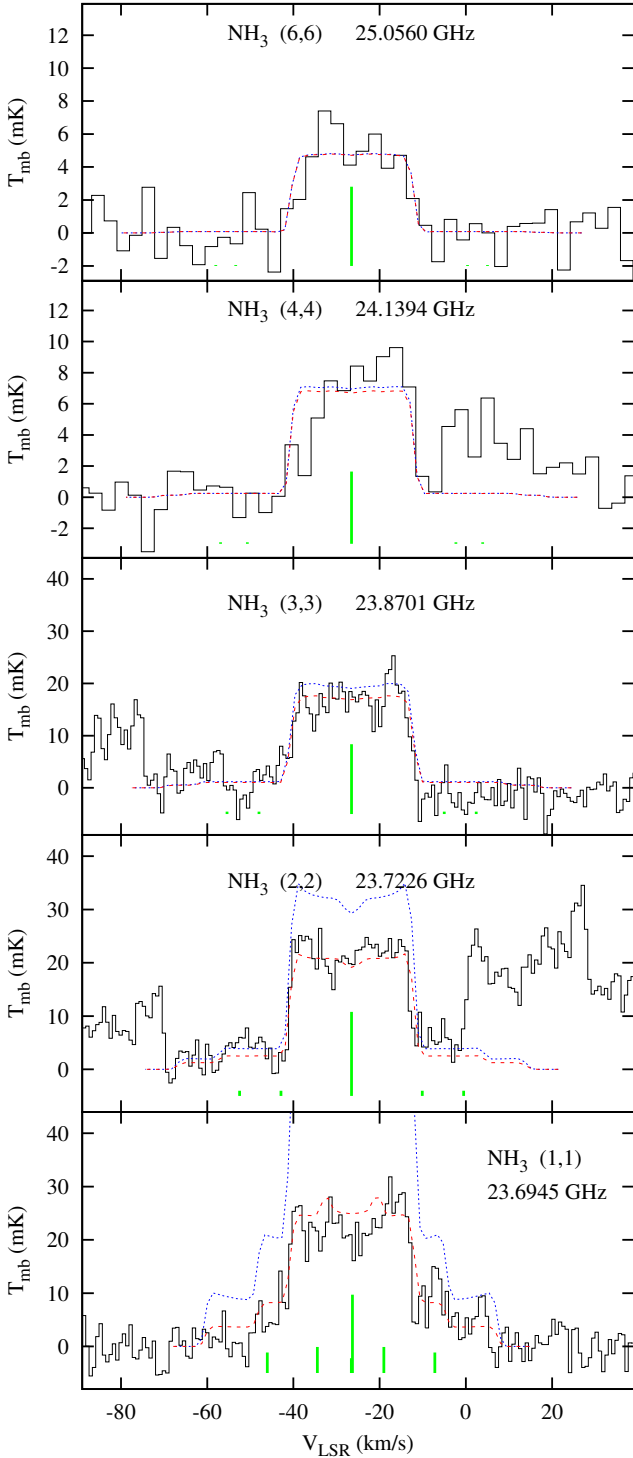


Fig. 6. Profiles of the inversion lines as computed for the best-fit models, which assume $R_{\text{ph}} = 3 \times 10^{16}$ cm and the T_{gas} distribution from [Crosas & Menten \(1997\)](#), (blue dotted lines) are overplotted on the observed inversion transitions (solid lines) from [Gong et al. \(2015\)](#). Theoretical profiles for the same T_{gas} profile, but with the photodissociation radius reduced to $R_{\text{ph}} = 1.5 \times 10^{16}$ cm are shown with red dashed lines. Vertical sticks show positions and relative intensities of hyperfine components.

disagreement with the $aQ(6, 6)$ line is most probably due to the neglect of the inner velocity structure of the envelope or to a higher value of the formation radius.

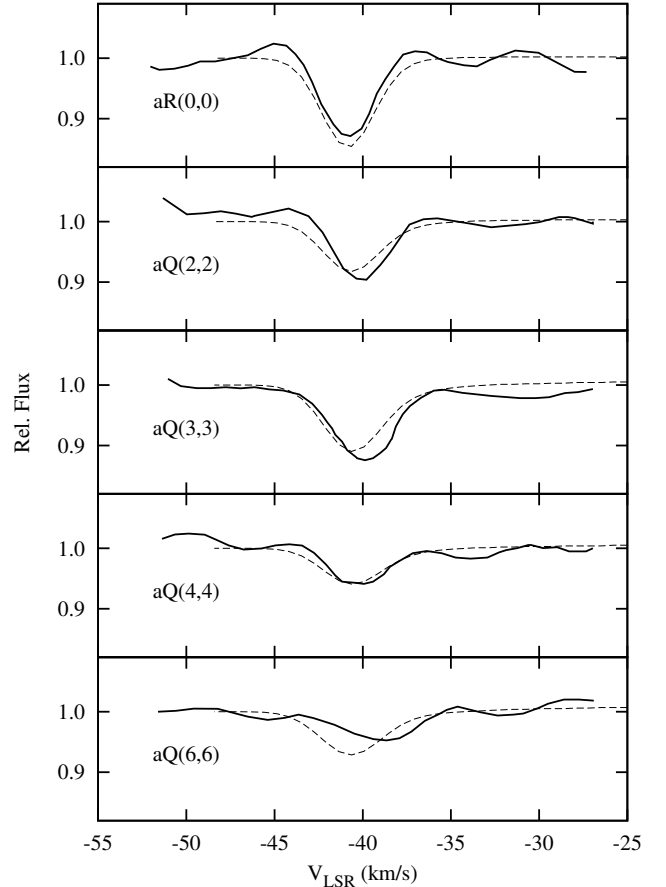


Fig. 7. Profiles of NH_3 lines in the ν_2 band observed by [Keady & Ridgway \(1993\)](#) (solid lines) and synthesized profiles using data from the best-fit models (dashed lines). Theoretical lines have been convolved with a Gaussian profile to achieve a spectral resolution of 2.9 km s^{-1} .

5. Discussion

5.1. Abundance of ammonia

Over the past 30 yr, the determination of the NH_3 abundance in the envelope of IRC+10216 has been the subject of observational studies at radio, mid-infrared, and submillimeter wavelengths. All these observations appeared to provide divergent abundances but, as we discuss below, the main reason for the different results comes from the inclusion (or not) of radiative pumping to the vibrational levels and differences in column densities.

Prior to this study, the only observation of a NH_3 rotational transition was made with the spectrograph on board the *Odin* satellite ([Hasegawa et al. 2006](#)). The rather poor signal-to-noise ratio obtained for the lowest $1_0(s)-0_0(a)$ transition of ortho- NH_3 did not provide a precise measurement of the line profile. The ammonia abundance relative to H_2 was determined as being 1×10^{-6} , significantly above our determination, $f(\text{ortho-}\text{NH}_3) = 2.8 \times 10^{-8}$. However, the analysis of the line was based on a simplified model of a single $K = 0$ ladder, limited to the ground vibrational state and, more importantly, neglecting radiative pumping by the infrared radiation. For the adopted model of the IRC+10216 envelope, results from our code show that, with the neglect of IR pumping the abundance of ammonia has to be increased by factor of about 20 to explain the measured $1_0(s)-0_0(a)$ line flux. In addition, the line profile becomes parabolic, which is characteristic of unresolved optically thick

emission, in disagreement with the profiles observed by *Herschel*. Thus, we can conclude that the largest discrepancy in the determination of the ammonia abundance seems to be resolved. The effect of infrared pumping on the molecular abundances derived for evolved stars was previously noted in the paper of Agúndez & Cernicharo (2006), who show that by including the ν_2 mode of H₂O the abundance of water was decreased by a factor of ≥ 10 with respect to that derived assuming pure rotational excitation. For the specific case of NH₃, Schöier et al. (2011) have shown that taking into account IR pumping via vibrationally excited states will decrease the abundance of ammonia by an order of magnitude. In addition, Danilovich et al. (2014) have derived the abundance of ammonia in the S-type star W Aql, including the ν_2 state in their analysis of the radiative transfer.

The early observations of the (1, 1) and (2, 2) inversion transitions of para-NH₃ around 23 GHz were made by Kwok et al. (1981), Bell et al. (1982), and Nguyen-Q-Rieu et al. (1984). For their assumed distance of 200 pc and mass loss rate of $2 \times 10^{-5} M_{\odot} \text{ yr}^{-1}$, they found $f(\text{para-NH}_3)$ as being between 3×10^{-8} and 2×10^{-8} . At the distance of 130 pc adopted here, and for optically thin transitions, the corresponding values of $f(\text{para-NH}_3)$ are 0.8×10^{-8} and 0.5×10^{-8} , respectively, for the assumed mass loss rate of 3.25×10^{-5} . The estimates are a factor of 4 to 6 lower than our determination of para-NH₃ abundance, namely $(3.2^{+0.7}_{-0.6}) \times 10^{-8}$. This difference may be due to simplifying assumptions made in the derivation of the ammonia abundance in these earlier papers. Recently, Gong et al. (2015) have inferred the abundances of ortho- and para-NH₃ from observations of their metastable inversion transitions (J, K) = (1, 1), (2, 2), (3, 3), (4, 4), (6, 6). They lie between 7.1×10^{-8} to 1.4×10^{-7} for ortho-NH₃, and between 1.1×10^{-7} and 1.3×10^{-7} for para-NH₃. Here, the assumed mass-loss rate was $2 \times 10^{-5} M_{\odot}$ so, for our adopted mass loss rate, the abundances correspond to values from 4.4×10^{-8} to 8.6×10^{-8} for ortho-NH₃ and from 6.8×10^{-8} to 8.0×10^{-8} for para-NH₃. Moreover, these values are dependent on the column density of molecular hydrogen, which is uncertain by a factor of 2 (Gong et al. 2015).

Observations of mid-IR ν_2 transitions in absorption performed by Betz et al. (1979), Keady & Ridgway (1993) have yielded another estimate of the total abundance of ammonia. For an assumed mass-loss rate of $2 \times 10^{-5} M_{\odot} \text{ yr}^{-1}$, these two studies inferred total ammonia abundances of 1×10^{-7} and 1.7×10^{-7} , respectively. Rescaled to our adopted mass-loss rate, these values transform to 6×10^{-8} and 1×10^{-7} , in agreement with the total ammonia abundance derived by us $f(\text{NH}_3) = (6.0 \pm 0.6) \times 10^{-8}$.

Finally, we note that the remaining differences – at a factor of a few – between the NH₃ abundances determined by various methods may not be so significant. The determination of the NH₃ abundances using mid-IR absorption ν_2 transitions requires an assumption for the column density of ammonia. The values range from about $2 \times 10^{15} \text{ cm}^{-2}$ (Betz et al. 1979; Keady & Ridgway 1993) to $8 \times 10^{15} \text{ cm}^{-2}$ (Monnier et al. 2000). This may be compared to the total column density along the sight line to the central star in our best-fit model, $1.5 \times 10^{16} \text{ cm}^{-2}$. The different observations average the column density over different parts of the envelope and therefore probe different regions of the CSE. We note that the column density is very sensitive to the densest inner parts of the envelope. For example, for our model with constant velocity and with $R_f = 10 R_{\star}$ the total column density drops to only $5 \times 10^{15} \text{ cm}^{-2}$. The assumed velocity profile in the acceleration zone also plays a role. For example, Monnier et al. (2000) had to assume a much higher column density of $8 \times 10^{15} \text{ cm}^{-2}$, by modifying only the behaviour of

the velocity field in the inner part of the envelope, while using the model of the dusty envelope similar to the original one from Keady & Ridgway (1993).

5.2. Ammonia formation radius

The best-fit models for ortho- and para-NH₃, marked by + signs on the middle and on the right panels of Fig. 5, respectively, are obtained for $R_f = 1.0 \times 10^{14} \text{ cm}$ or $2.5 R_{\star}$. This means that a lower limit on the ammonia formation radius is not provided by our model fits. On the other hand, the distribution of contours for 1, 2, and 3 σ levels on these panels show that ammonia cannot be formed too far from the stellar photosphere. At the 1 σ level, the upper limit on the formation radius must be at most $20 R_{\star}$, while at the 2 σ level it is around $35 R_{\star}$. This seems to be in rough agreement with the formation radius of ammonia as estimated by Keady & Ridgway (1993) and Monnier et al. (2000) on the basis of their analysis of mid IR lines. The analysis of Keady & Ridgway (1993) allows a distance closer than $10 R_{\star}$, whereas Monnier et al. (2000) conclude that ammonia is formed at a distance $\geq 20 R_{\star}$. This last conclusion was based on interferometric observations of the mid-IR bands in the continuum and at line centre and further modelling of the ratio of visibility functions.

The rotational line profiles of NH₃ were fit assuming that the velocity field is constant. However, we performed test computations with the gas velocity field inside the envelope used by Crosas & Menten (1997). We found that they produce a narrow emission feature in the centre of the highest rotational and inversion transitions that are not seen in the observed line profiles. To remove this feature, created by the acceleration region, it was necessary to constrain the formation radius by shifting R_f above 5–10 R_{\star} , although the quality of the fit – as measured by χ^2_{red} – was worse in this case. Nevertheless, it seems that the more realistic gas velocity field suggests that ammonia is not formed at the stellar photosphere as suggested by our formal fit to the rotational transitions, assuming a constant outflow velocity.

5.3. Photodissociation radius

The photodissociation radius has been constrained by observations of the of the NH₃ (1, 1) and (2, 2) inversion lines (Nguyen-Q-Rieu et al. 1984). Their analysis of the observed lines required a cut-off of the molecular abundance beyond a radius of $(0.6\text{--}1) \times 10^{17} \text{ cm}$ at the assumed distance of 200 pc. This corresponds to $(4.0\text{--}6.5) \times 10^{16} \text{ cm}$ at distance assumed in this paper, $d = 130 \text{ pc}$, and is in the range allowed by our modelling, $R_{\text{ph}} > 2\text{--}3 \times 10^{16} \text{ cm}$. Models for the NH₃ distribution in the circumstellar envelope of IRC+10216 presented by Decin et al. (2010), and shown by the dotted line in Fig. 3, predict a decrease in the ammonia abundance in the outer envelope that is more rapid than is allowed by the observations. With this type of distribution, we cannot fit the rotational lines of ammonia, especially the lowest transition of ortho-NH₃, since its upper level is underpopulated at still quite high gas temperatures (see Figs. 1 and 3). Similarly, this is also the case for the reduced photodissociation radius inferred from the fit to the observations of inversion lines by Gong et al. (2015).

5.4. Line shapes

Thanks to the high signal-to-noise ratio (S/N) obtained for the ortho-NH₃ $1_0(s)\text{--}0_0(a)$ spectrum, the details of the line profile

are well-constrained (see bottom left panel in Fig. 2). Another line, the $3_2(s)-2_2(a)$ line at 1763.823 GHz, was also observed at a high S/N ratio and has an identical shape (see the middle right panel in Fig. 2). The energy of the upper level for these two transitions is quite different (29 and 127 K, see Table 1), and the similarity of their shapes suggests that both of them are excited in a rather similar region within the envelope. Surprisingly, their shapes show two peaks resembling the profiles of resolved optically thin transitions. However, this is not possible because, given the *Herschel* beam size at the frequency of the $1_0(s)-0_0(a)$ transition, it would require an outer radius for the ammonia-emitting region to be in excess of 10^{17} cm, a value close to the CO photodissociation radius. Very similar shapes of rotational lines of SiO ($J = 2-1$ through $J = 7-6$ in their ground vibrational state) have been observed in IRC+10216 with the IRAM 30-m telescope by Agúndez et al. (2012) (see their Fig. 4), who suggested that the observed peaks may be formed by additional excitation provided by shells with enhanced density observed in the outer layers of the envelope of IRC+10216 (see e.g. Cernicharo et al. 2015). The line shape can also indicate the presence of spiral shells (Decin et al. 2015) in the inner envelope, and/or a hole in the middle of the envelope in the ammonia distribution.

Another possible hypothesis that explains the slightly double-peaked shape of NH_3 rotational transitions could be additional excitation of levels by line overlap. In particular, this effect may couple ortho- and para- NH_3 levels. This hypothesis has been tested by simultaneous computations of both ortho and para species including effects of line overlap. We found, however, that this process cannot explain the asymmetric double-peak line profiles that are observed. On the other hand, it does reproduce the resulting composite profile of the overlapping transitions (para- NH_3 $3_1(s)-2_1(a)$ at 1763.601 GHz and ortho- NH_3 $3_0(s)-2_0(a)$ at 1763.524 GHz) shown in Fig. 2 by the long dash line.

The theoretical profiles for the inversion transitions show a complex structure, due to the overlap of emission in the hyperfine components. In particular, the profile of the para- NH_3 (1, 1) line (see the lowest panel in the Fig. 6) shows at least the central and the two long wavelength components of the hyperfine multiplet. The two narrow peaks at -32 and -20 km s^{-1} caused by the overlap of the blue edge of one component and red edge of the next one further confirms the presence of at least one of the short wavelength components. Observations with higher S/N would probably reveal the shortest wavelength component.

6. Summary

We present *Herschel*/HIFI observations obtained with high spectral resolution for all nine rotational transitions up to the $J = 3$ levels for ortho- and para- NH_3 in the envelope of the C-rich AGB star IRC+10216. Using our numerical code MOLEXCSE, which solves the non-LTE radiative transfer in molecular lines and dust continuum, we searched for the best-fit parameters that explain all three ortho- and six para- NH_3 rotational lines. Computations were done separately for ortho- and para- NH_3 . Three free parameters were constrained by the modelling effort: the ammonia formation radius, its photodissociation radius and the abundance. The best fits were obtained when infrared pumping of NH_3 was included, using the gas temperature structure from Crosas & Menten (1997), which is representative of self-consistently computed T_{gas} structures. Test computations with the gas temperature profile of De Beck et al. (2012) showed that, while the fit obtained is slightly worse, the best-fit

parameters are only weakly sensitive to the assumed temperature structure.

We found that the best fit to the rotational lines is obtained if the abundance of ortho- and para- NH_3 are equal to $(2.8 \pm 0.5) \times 10^{-8}$ and $(3.2^{+0.7}_{-0.6}) \times 10^{-8}$, respectively. The fit, including both rotational and inversion lines, gives the ortho- and para- NH_3 abundances that are quite similar (within the error bars) to those obtained from the analysis limited to the rotational lines only ($f(\text{ortho-NH}_3) = (2.4 \pm 0.4) \times 10^{-8}$ and $f(\text{para-NH}_3) = (3.2 \pm 0.5) \times 10^{-8}$). These values are compatible with an ortho/para ratio of one, characteristic for the formation of ammonia at high temperatures. The derived abundance of ortho- NH_3 has solved the long-lasting problem of the discrepancy between the abundance derived from the lowest submillimeter rotational line and those from radio inversion or infrared absorption transitions. It was found that the main process that brought the abundances of ammonia derived from different spectral transitions close to each other was the inclusion of the NIR radiative pumping of ammonia via the $10 \mu\text{m } \nu_2 = 1$ band. The average abundance of NH_3 derived from rotational lines agree to within of a factor a few with those from radio inversion or infrared absorption transitions, and we argued that this difference may not be significant, since both methods rely on an uncertain determination of the ammonia column density.

In addition, since the MOLEXCSE code also offers predictions for other NH_3 transitions in the radio and mid-IR range, we tested whether our best-fit models were able to explain the observations of Gong et al. (2015) and Keady & Ridgway (1993). In the case of the inversion transitions, we found that reducing R_{ph} to 1.5×10^{16} cm gives a very good fit to the lower para- NH_3 (1, 1) and (2, 2) inversion transitions, but with so small a R_{ph} that the fit to the rotational lines of ortho- NH_3 is significantly worse. We admit, however, that our best fit model for the rotational transitions may overpredict the envelope size as a result of inaccuracies in modelling of the inner parts of the envelope. In the case of the MIR absorption lines, we found that our best-fit model reproduces the observed profiles from Keady & Ridgway (1993) fairly well. Some disagreement with the $aQ(6, 6)$ line profile is most probably due to our neglect of the inner velocity structure in the envelope.

The ammonia formation radius is not well-constrained in our approach, and the best fitting abundances of ortho- and para- NH_3 were obtained at the minimum value of the formation radius considered in our analysis, $2.5 R_{\star}$. The best fits were obtained assuming that the outflow velocity is constant, so we performed test computations with the gas velocity, increasing inside the acceleration zone. We found that for $R_f = 2.5 R_{\star}$ this type of velocity field produces a narrow emission feature in the centre of the highest inversion transitions that is not seen in the observed line profiles. To remove this feature, created in the acceleration region, it was necessary to shift R_f above $5-10 R_{\star}$, still inside the 1σ limits obtained from fitting the line strengths. Nevertheless, the more realistic gas velocity field suggests that ammonia is not formed at the stellar photosphere as had been suggested by the formal fits to the rotational transitions, assuming a constant gas velocity field.

A lower limit on the ammonia photodissociation radius seems to be implied by our fit to the rotational transitions, while the maximum value for R_{ph} is unconstrained. Our value of $(2-3) \times 10^{16}$ cm seems to agree quite well with other determinations. However, the best fit to the both rotational and inversion transitions does not give fully consistent results for the ortho- ($R_{\text{ph}} = (5^{+1}_{-3}) \times 10^{16}$ cm) and para- NH_3

($R_{\text{ph}} = (1.5 \pm 0.2) \times 10^{16}$ cm). Furthermore, a distribution of NH₃ with the fast decrease predicted by the model of Decin et al. (2010) does not yield a good fit to the lowest rotational transitions of ortho-ammonia.

The two rotational lines that have the highest S/N ($1_0(s)-0_0(a)$ of ortho- at 572.498 GHz and $3_1(s)-2_1(a)$ of para-NH₃ at 1763.601 GHz) show two asymmetric peaks in their profile. These can be due to an excess of radiation from almost concentric rings or spiral shells as suggested in literature. We also investigated the possibility that they result from the coupling of the ortho- and para-NH₃ levels by the effects of line overlap. The computations showed that this process cannot explain the observed peaks, but it can successfully account for the $3_1(s)-2_1(a)$ at 1763.601 GHz and ortho-NH₃ $3_0(s)-2_0(a)$ line at 1763.524 GHz.

Acknowledgements. M.S.c. and R.S.z. acknowledge support by the National Science Center under grant (N 203 581040). J.H.e. thanks the support of the NSFC research grant No. 11173056. Funded by Chinese Academy Of Sciences President's International Fellowship Initiative. We acknowledge support from EU FP7-PEOPLE-2010-IRSES programme in the framework of project POSTAG-BinGALAXIES (Grant Agreement No. 269193). Grant No. 2015VMA015. V.B., J.A. and P.P. acknowledge support by the Spanish MICINN, program CONSOLIDER INGENIO 2010, grant "ASTROMOL" (CSD2009-00038), and MINECO, grants AYA2012-32032 and FIS2012-32096. J. Cernicharo thanks Spanish MINECO for funding under grants AYA2009-07304, AYA2012-32032, CSD2009-00038, and ERC under ERC-2013-SyG, G.A. 610256 NANOCOSMOS. L.D. acknowledges funding by the European Research Council under the European Community's H2020 program/ERC grant agreement No. 646758 (AEROSOL). K.J. acknowledges the funding from the Swedish national space board. D.A.N. was supported by a grant issued by NASA/JPL. HIFI has been designed and built by a consortium of institutes and university departments from across Europe, Canada and the United States under the leadership of SRON Netherlands Institute for Space Research, Groningen, The Netherlands and with major contributions from Germany, France and the US. Consortium members are: Canada: CSA, U.Waterloo; France: CESR, LAB, LERMA, IRAM; Germany: KOSMA, MPIfR, MPS; Ireland, NUI Maynooth; Italy: ASI, IFSI-INAF, Osservatorio Astrofisico di Arcetri- INAF; Netherlands: SRON, TUD; Poland: CAMK, CBK; Spain: Observatorio Astronómico Nacional (IGN), Centro de Astrobiología (CSIC-INTA); Sweden: Chalmers University of Technology – MC2, RSS & GARD; Onsala Space Observatory; Swedish National Space Board, Stockholm University – Stockholm Observatory; Switzerland: ETH Zurich, FHNW; USA: Caltech, JPL, NHSC. HCSS/HSpot/HIPE is a joint development by the *Herschel* Science Ground Segment Consortium, consisting of ESA, the NASA *Herschel* Science Center, and the HIFI, PACS and SPIRE consortia.

References

- Agúndez, M., & Cernicharo, J. 2006, *ApJ*, **650**, 374
 Agúndez, M., Cernicharo, J., & Guélin, M. 2010, *ApJ*, **724**, L133
 Agúndez, M., Fonfría, J. P., Cernicharo, J., et al. 2012, *A&A*, **543**, A48
 Becklin, E. E., Frogel, J. A., Hyland, A. R., Kristian, J., & Neugebauer, G. 1969, *ApJ*, **158**, L133
 Bell, M. B., Kwok, S., & Feldman, P. A. 1980, in *Interstellar Molecules*, ed. B. H. Andrew, *IAU Symp.*, **87**, 495
 Bell, M. B., Kwok, S., Matthews, H. E., & Feldman, P. A. 1982, *AJ*, **87**, 404
 Betz, A. 1987, in *Astrochemistry*, eds. M. S. Vardya, & S. P. Tarafdar, *IAU Symp.*, **120**, 327
 Betz, A. L., McLaren, R. A., & Spears, D. L. 1979, *ApJ*, **229**, L97
 Bunker, P. R., & Jensen, P. 1998, *Molecular symmetry and spectroscopy*, 2nd edn. (Ottawa, Canada: NRC Research Press)
 Cernicharo, J., Marcelino, N., Agúndez, M., & Guélin, M. 2015, *A&A*, **575**, A91
 Cherchneff, I. 2012, *A&A*, **545**, A12
 Cheung, A. C., Rank, D. M., Townes, C. H., Thornton, D. D., & Welch, W. J. 1968, *Phys. Rev. Lett.*, **21**, 1701
 Crosas, M., & Menten, K. M. 1997, *ApJ*, **483**, 913
 Danby, G., Flower, D. R., Valiron, P., Schilke, P., & Walmsley, C. M. 1988, *MNRAS*, **235**, 229
 Danilovich, T., Bergman, P., Justtanont, K., et al. 2014, *A&A*, **569**, A76
 De Beck, E., Lombaert, R., Agúndez, M., et al. 2012, *A&A*, **539**, A108
 de Graauw, T., Helmich, F. P., Phillips, T. G., et al. 2010, *A&A*, **518**, L6
 Decin, L., Hony, S., de Koter, A., et al. 2006, *A&A*, **456**, 549
 Decin, L., Agúndez, M., Barlow, M. J., et al. 2010, *Nature*, **467**, 64
 Decin, L., Richards, A. M. S., Neufeld, D., et al. 2015, *A&A*, **574**, A5
 Gong, Y., Henkel, C., Spezzano, S., et al. 2015, *A&A*, **574**, A56
 Groenewegen, M. A. T., van der Veen, W. E. C. J., & Matthews, H. E. 1998, *A&A*, **338**, 491
 Groenewegen, M. A. T., Barlow, M. J., Blommaert, J. A. D. L., et al. 2012, *A&A*, **543**, L8
 Harju, J., Walmsley, C. M., & Wouterloot, J. G. A. 1993, *A&AS*, **98**, 51
 Hasegawa, T. I., Kwok, S., Koning, N., et al. 2006, *ApJ*, **637**, 791
 Herbig, G. H., & Zappala, R. R. 1970, *ApJ*, **162**, L15
 Ho, P. T. P., & Townes, C. H. 1983, *ARA&A*, **21**, 239
 Jijina, J., Myers, P. C., & Adams, F. C. 1999, *ApJS*, **125**, 161
 Keady, J. J., & Ridgway, S. T. 1993, *ApJ*, **406**, 199
 Kirsanova, M. S., Wiebe, D. S., Sobolev, A. M., Henkel, C., & Tsvilev, A. P. 2014, *MNRAS*, **437**, 1593
 Kukulich, S. G. 1967, *Phys. Rev.*, **156**, 83
 Kwok, S., Bell, M. B., & Feldman, P. A. 1981, *ApJ*, **247**, 125
 Le Bertre, T. 1992, *A&AS*, **94**, 377
 Mamon, G. A., Glassgold, A. E., & Huggins, P. J. 1988, *ApJ*, **328**, 797
 McLaren, R. A., & Betz, A. L. 1980, *ApJ*, **240**, L159
 Men'shchikov, A. B., Balega, Y., Blöcker, T., Osterbart, R., & Weigelt, G. 2001, *A&A*, **368**, 497
 Menten, K. M., Wyrowski, F., Alcolea, J., et al. 2010, *A&A*, **521**, L7
 Menten, K. M., Reid, M. J., Kamiński, T., & Claussen, M. J. 2012, *A&A*, **543**, A73
 Mihalas, D., Kunasz, P. B., & Hummer, D. G. 1975, *ApJ*, **202**, 465
 Miller, J. S. 1970, *ApJ*, **161**, L95
 Monnier, J. D., Danchi, W. C., Hale, D. S., Tuthill, P. G., & Townes, C. H. 2000, *ApJ*, **543**, 868
 Mueller, M., Jellema, W., Olberg, M., Moreno, R., & Teyssier, D. 2014, *The HIFI Beam: Release 1, Release Note for Astronomers*, Tech. Rep. HIFI-ICC-RP-2014-001, v1.1, HIFI-ICC
 Neufeld, D. A., González-Alfonso, E., Melnick, G., et al. 2010, *A&A*, **521**, L5
 Neufeld, D. A., Tolls, V., Agúndez, M., et al. 2013, *ApJ*, **767**, L3
 Nguyen-Q-Rieu, Graham, D., & Bujarrabal, V. 1984, *A&A*, **138**, L5
 Nguyen-Q-Rieu, Winnberg, A., & Bujarrabal, V. 1986, *A&A*, **165**, 204
 Osorio, M., Anglada, G., Lizano, S., & D'Alessio, P. 2009, *ApJ*, **694**, 29
 Pegourie, B. 1988, *A&A*, **194**, 335
 Pilbratt, G. L., Riedinger, J. R., Passvogel, T., et al. 2010, *A&A*, **518**, L1
 Roelfsema, P. R., Helmich, F. P., Teyssier, D., et al. 2012, *A&A*, **537**, A17
 Rouleau, F., & Martin, P. G. 1991, *ApJ*, **377**, 526
 Rydbeck, O. E. H., Sume, A., Hjalmarsen, A., et al. 1977, *ApJ*, **215**, 35
 Schoenberg, K., & Hempe, K. 1986, *A&A*, **163**, 151
 Schöier, F. L., & Olofsson, H. 2001, *A&A*, **368**, 969
 Schöier, F. L., Ryde, N., & Olofsson, H. 2002, *A&A*, **391**, 577
 Schöier, F. L., van der Tak, F. F. S., van Dishoeck, E. F., & Black, J. H. 2005, *A&A*, **432**, 369
 Schöier, F. L., Maercker, M., Justtanont, K., et al. 2011, *A&A*, **530**, A83
 Szczerba, R., Omont, A., Volk, K., Cox, P., & Kwok, S. 1997, *A&A*, **317**, 859
 Thaddeus, P., Krisher, L. C., & Loubser, J. H. N. 1964, *J. Chem. Phys.*, **40**, 257
 Truong-Bach, Nguyen-Q-Rieu, Omont, A., Olofsson, H., & Johansson, L. E. B. 1987, *A&A*, **176**, 285
 Truong-Bach, Morris, D., & Nguyen-Q-Rieu. 1991, *A&A*, **249**, 435
 Umamoto, T., Mikami, H., Yamamoto, S., & Hirano, N. 1999, *ApJ*, **525**, L105
 Walmsley, C. M., & Ungerechts, H. 1983, *A&A*, **122**, 164
 Wiens, M., Wyrowski, F., Schuller, F., et al. 2012, *A&A*, **544**, A146
 Yurchenko, S. N., Barber, R. J., & Tennyson, J. 2011, *MNRAS*, **413**, 1828